Airflow profile study of a compost dairy barn using a low-cost 3D-printed anemometer network

F.A. Obando Vega[1,*], A.P. Montoya Rios[1], F.A. Damasceno[2],
J.A. Osorio Saraz[1] and J.A. Costa Do Nascimento[2]

[1]Universidad Nacional de Colombia sede Medellín, Facultad de Ciencias Agrarias, Departamento de Ingeniería Agrícola y Alimentos, CO050034 Medellín, Colombia
[2]Federal University of Lavras, Department of Engineering, BR37200-000 Lavras, Minas Gerais, Brazil
[*]Correspondence: faobando@unal.edu.co

Abstract. Mechanical ventilation is commonly used for environmental thermal regulation inside closed-field agricultural production systems. Analyzing the air distribution inside these facilities and the correct operation of the fans can be a challenging. This could be determined using cost prohibitive techniques as particle image velocimetry or deploying large wind sensors networks on-site. To avoid this limitation without a lack of measurement accuracy, this research was focused on developing and test a low-cost anemometer network based in low cost propeller's anemometers, built using fused 3D-printed and open-hardware platforms. Four propeller anemometers with three to six blades were simulated using the 6-DOF method of ANSYS computer fluid dynamics software. Similar results were obtained for all the simulated models with minor differences. Anemometers were tested in an open circuit wind tunnel before to be evaluated in two open compost dairy barn building using high-volume low-speed and low-volume high-speed fans. Data were analyzed by employing contour maps, descriptive statistics and correlation. The results show that the anemometer network determines the fan's wind profile for wind speeds over 0.7 m s^{-1} and it was possible to determine the facilities spots with ventilation problems. The proposed anemometer network and methodology are a good alternative to analyze the operating conditions of the tested agricultural facilities and optimize its performance.

Key words: ventilation optimization; CFD; wind tunnel; Arduino; sensor network; directional anemometer; compost barn.

INTRODUCTION

The air quality and homogeneity inside closed-field agricultural production systems such as greenhouses and plant factories (R.R. Shamshiri et al., 2018) depends on a good natural and mechanical ventilation. In order to have a suitable environment for the development of agricultural practices, adequate ventilation rates and air distribution are needed (Samer et al., 2011). The behavior of the airflow inside those facilities have been evaluated employing different techniques: Computer Fluid Dynamics (*CFD*) simulations, tracer gas and anemometer networks, among others. Being the last ones cost prohibitive (Fiedler et al., 2013; van Dooren & Sapounas, 2013; Bustamante et al., 2015). The characterization of airflow distribution in mechanical ventilated installations,

employing these techniques, allows to evaluate the performance of the ventilation system (R. Shamshiri & Ismail, 2012).

In particular, compost dairy barns are facilities that require an adequate control of the ventilation rates and air distribution in order to guarantee the compost drying homogeneity, the livestock bioclimatic comfort and proper management of gas emissions. The number of fans and its location in these facilities depend of the livestock density (Black et al., 2013) regardless the compost ventilation requirements. This kind of installations would benefit of the inside air distribution analysis near to the floor surface. No scientific publication related with the evaluation of the ventilation rate over the compost drying process was found. Air distribution analysis are also an important tool in modern greenhouses to characterize its ventilation and its relation with the microclimatic variables, several references in this matter can be found in literature (R. Shamshiri, 2017).

The low ventilation rates in closed-field agricultural facilities limits a uniform microclimate (R.R. Shamshiri et al., 2017), hence different types of anemometers are used for measuring air velocity. The most used types are the hot wire and the ultrasonic ones, which are some of the most expensive ones (Gao et al., 2016). Therefore, its implementation in sensor networks, composed by several anemometers, is limited. Hence, the rate and air profiles in these type of installations have been done mostly with CFD simulation (Zajicek & Kic, 2012; van Dooren & Sapounas, 2013; Vilela et al., 2019) and/or employing the tracer gas technique. In this matter, the tracer gas technique was used to compute the ventilation rate in two naturally ventilated dairy barns (Kiwan et al., 2012) with good results. While Calvet et al. (2010) found that the tracer gas technique underestimated the measurement when comparing with the direct measurement of the ventilation rate. However, van Dooren & Sapounas (2013) developed CFD simulations models to improve tracer gas techniques to measure the ventilation rate and pattern flow of from naturally ventilated livestock buildings with good agreement between measured data and computational results.

Mechanical anemometers are the most commonly used sensor for wind velocity measurement in climatic applications (Pindado et al., 2012). Among them, the low friction propeller anemometers are the most suitable for measuring low wind velocities, because their low starting speed and being less prone to overspending (Camuffo, 2019). Due to the elevated cost and measurement complexity of the air velocity implementation in real scale facilities (Luck et al., 2014; Bustamante et al., 2017) , it is imperative to have low cost anemometer sensor networks that allows the study of air distribution in agricultural facilities. Particularly in the case of compost dairy barns facilities, it is necessary to study the behavior of the air near the floor to ensure an efficient drying rate of the compost.

Using 3-D printing it is possible to develop anemometers with specific characteristics for wind speed measurement in closed-field agricultural production systems. In this issue Leoni et al. (2018) developed an spherical anemometer, with 0 to 20 m s^{-1} range of measurement using a 3D-printed with good results. Employing low-cost development platforms, it is possible to implement measurement systems for acquiring data from multiple sensors simultaneously, as it did (Obando Vega et al., 2020). In this area, (Gao et al., 2016) developed and low cost omnidirectional anemometer, based on Arduino platform, with measurement range of 0 to 6 m s^{-1} for multipoint measurement applications. The developed anemometer sensor network could

be used to characterize wind behavior in agricultural facilities or ventilation systems, as was proposed by (Samer et al., 2011).

The developed anemometers can be calibrated in wind tunnels, as proposed by (Pindado et al., 2012), who studied the calibration of several mechanical anemometers, employing this technique. The aerodynamic behavior of the low-cost sensors could be studied using CFD simulation employing models with 6 degrees of freedom (CFD/6-DOF). This technique has been used by several authors to study the dynamics of the movement of a solid body against a fluid or vice versa. This novel technique has been applied to evaluations of wind turbines by several authors (Dunbar et al., 2015).

In the present work is proposed: (1) to develop four types of low-cost propeller's anemometers, using a 3D-printed and open-source development platform (www.arduino.cc); (2) to study the dynamic behavior of the anemometers using CFD/6-DOF simulation, in order to evaluate their performance and select the most suitable instrument for measuring low wind speeds, by comparing its Root Mean Square Errors (RMSE) and settling times; (3) to calibrate the anemometers in an open circuit wind tunnel; (4) to implement a network of 10 sensors for the measurement of airflow velocity speed profiles using the anemometer model with the best performance; and (5) to study the air distribution in two compost dairy barns with mechanical ventilation, establishing the speed profiles near the ground surface and the air homogeneity distribution at compost surface.
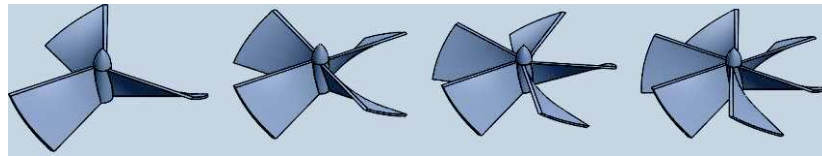
MATERIALS AND METHODS

CFD analysis

Figure 1. Propeller design with CAD software using different number of blades.

Four propeller anemometers of 150 mm of diameter and different number of blades (3 to 6) were designed employing SOLIDWORKS® CAD software (Fig. 1). The rotation speed of each propeller for specific airflow velocities were determined by mean of the ANSYS® R17.0 computer fluid dynamics (CFD) software using the dynamic mesh method and the 6-DOF solver (Ansys Inc., 2016) through simulations in transient state. ANSYS Fluent software was employed to solve the CFD model with convergence criteria of 1×10^{-3}. In order to determine differences between the propellers and to select the best suitable configuration, an airflow velocity of $1 \, \text{m s}^{-1}$ was established for the CFD simulations. A cylindrical shape around the propeller was considered as control volume of the CFD simulation, with 300 mm of diameter, 300 mm upstream and 500 mm downstream. In order to improve the CFD meshing process, the control volume were divided in four parts (Fig. 2), the first one enclosure the propeller surface, the second included the air flow around the propeller, finally the third and fourth ones include the upstream and downstream flow from the propeller. For the purpose to capture the

dynamics of the flow in the propeller surface, an inflation layer with a distance of 1×10^{-4} m from the surface, a growth rate of 1.2 and 5 layers maximum were implemented. A proximity and curvature mesh size function with a growth rate of 1.8 was used. To select the appropriate mesh size that gives a good balance between accuracy, computational time, and propeller rotation speed, a mesh sensibility analysis for the four-blade propeller was performed, for an airflow velocity of 1.5 m s^{-1} and three mesh sizes characterized by coarse, medium and fine relevant center sizes (Table 1). The orthogonal quality (> 1.0) and the skewness statistics (< 0.9) were used

Figure 2. Four-blade propeller ANSYS mesh.

to quantify the goodness of the meshing process and the differences between the CFD results and the running computational time help to select the best mesh sizes.
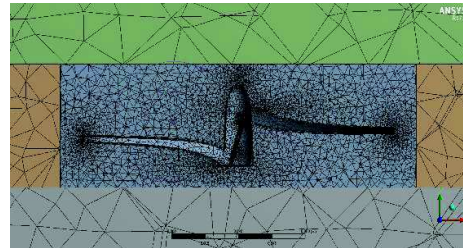
Table 1. Number of nodes, elements and statistics for the three mesh sizes used for the mesh sensibility analysis performed to the four-blade propeller

Mesh size		Coarse	Medium	Fine
Number of nodes		66767	70910	90379
Number of elements		212114	234177	325779
Orthogonal quality	Min	0.12543	0.11164	0.11161
	Max	0.99806	0.99664	0.99749
	Avg	0.7619	0.7663	0.79042
	SD	0.14297	0.1408	0.13299
Skewness	Min	5.604×10^{-6}	1.2217×10^{-6}	2.9459×10^{-6}
	Max	0.86132	0.88939	0.86896
	Avg	0.38199	0.37329	0.33801
	SD	0.16854	0.16931	0.16907

The k-ε RNG turbulence model and near-wall treatment were used to capture the dynamics of airflow near to the propeller surface. A first order implicit model for transient formulation and a SIMPLE scheme for pressure-velocity coupled were used as solutions methods. For the transient simulations, a small fixed step of 0.001 s was used for the entire simulation, starting with a time step of 0.0001 s for the first 20 iterations and then increasing the step size to 0.00015 s for the next 20 iterations, due to convergence issues. A Hewlett-Packard Z44 workstation desktop computer with four processors in parallel and one GPU was used to solve the CFD simulations.

The Normalized Mean Square Error (NMSE), as recommended by (ASTM, 2019) was employed to quantify the agreement between the CFD results and the experimental data. NMSE values less than 0.25 are accepted as good indicators of agreement.

Wind tunnel calibration test

ABS fused (Acrylonitrile Butadiene Styrene) 3D-printed models of the four propeller anemometers (Fig. 3, a), obtained with a height layer of 0.2 mm, were tested in an open circuit wind tunnel (Fig. 3, b). The propeller's axis rest on one ball bearing

(608ZZ) housed in an ABS 3D-printed support. The rotational speed of the propeller was measured using an encoder coupled to the propeller's axis (Fig. 3, c). The encoder was conformed by a perforated ABS 3D-printed wheel and a VISAY TCST2103 optical sensor (www.vishay.com), giving 15 pulses per propeller revolution. The number of pulses were determined with the low-cost open-source Arduino Nano microcontroller (www.arduino.cc). For this, a general purpose input and a timer interrupts were configured to count the number of pulses per second (*pps*) and converted it to revolution per minutes (RPM). The Arduino Nano can monitor two encoder simultaneously. Data was send every 10 s to a master station for recording in a micro-SD memory. This master station was conformed by an Arduino Mega 2560 with the capacity to receive data in real time from several anemometers employing the I^2C protocol (www.i2c-bus.org). The master station has a real time clock module (RTC DS3231-www.adafruit.com) for keeping track of time and an I^2C LCD for displaying purposes (Fig. 3, d). The open-circuit wind tunnel has a test area of 0.5 m width × 0.5 height m × 1 m large. It was composed by a *SIEMENS®* three-phase exhaust fan (*2CC2-634-5YB6T*), controlled with a 2 hp *SIEMENS SINAMICS V20®* variable frequency drive. A Gill WindSonic® ultrasonic anemometer (www.gillinstruments.com, ± 2% accuracy, 0 to 60 m s^{-1} range of measurement) was used as reference airflow velocity sensor. The airflow velocity was varied from 0 to 4.25 m s^{-1}. The experimental results were compared with the CFD simulations results.
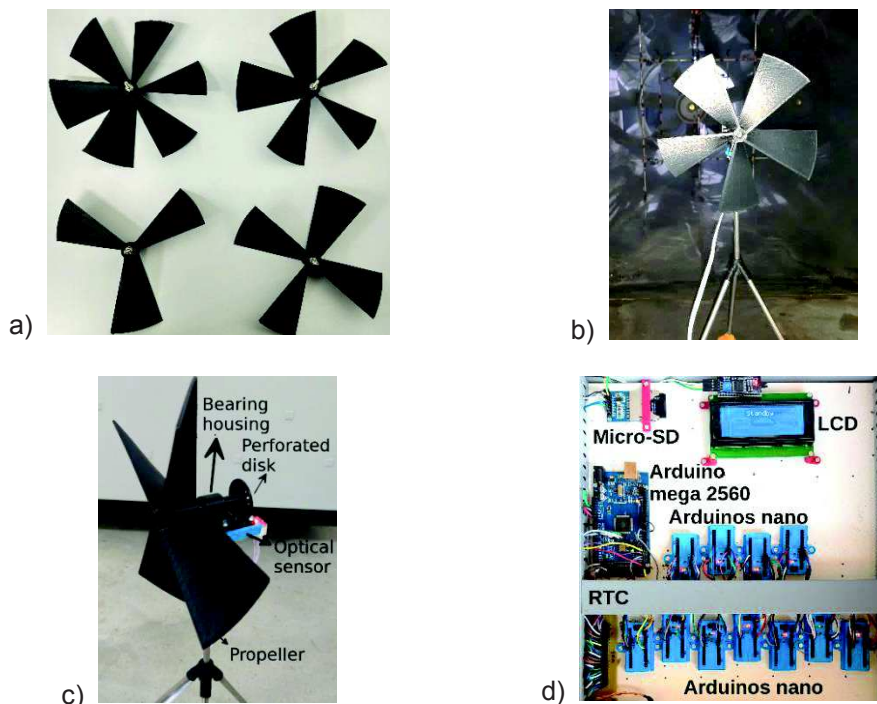

Figure 3. ABS 3D-printed propeller anemometers and datalogger system: a) Propeller with different number of blades tested; b) Five-blade propeller anemometer inside the open circuit wind tunnel; c) Propeller anemometer assembly; d) Master station components.

Compost dairy barn tests

An anemometer network composed by ten four-blade anemometers was implemented and installed in two cattle dairy buildings with compost barn bedded and mechanical ventilation. The network was used for determine the airflow velocity distribution at 0.3 m above the compost surface. The cattle dairy buildings were located in Brazil, in the state of Minas Gerais in the cities of Cláudio (Fig. 4, a, 20°24'38.8"S 44°36'51.4"W, dimensions of 19×49×4 m) and Perdões (Fig. 4, b, 21°06'28.5"S 45°02'09.8"W, dimensions of 20×40×4 m), employing high-volume low-speed (HVLS) fans (7.5 m diameter, 2 hp, operating at 70% of its rotation speed by means of a SIEMENS SYNAMICS V20® variable frequency driver) and low-volume high-speed (LVHS) fans (1.6 m of diameter, 1.5 hp), respectively. Both ventilation systems were installed in the ceiling of the facilities. For one HVLS fan, a measurement area of 13.8×10 m was defined and the network of anemometers was distributed in a row along the 13.8 m axis. For one LVHS fan, a measurement area of 10.8×10 m was defined in front of the fan and the network of anemometers was distributed in a row along the 10.8 m axis. For both fans, six tests locations along the 10 m axis were performed, where the anemometers are moved after two minutes of data recorder after its settling time. The propellers were oriented to the predominant wind direction on each location.
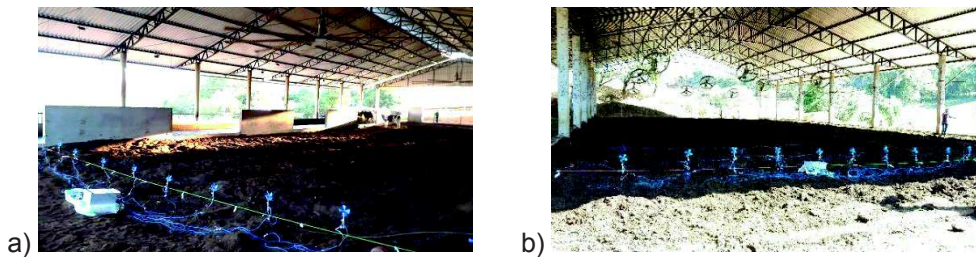

Figure 4. Distribution of the anemometer network in the cattle dairy buildings with compost barn: a) High-volume low-speed fans; b) Low-volume high-speed fans.

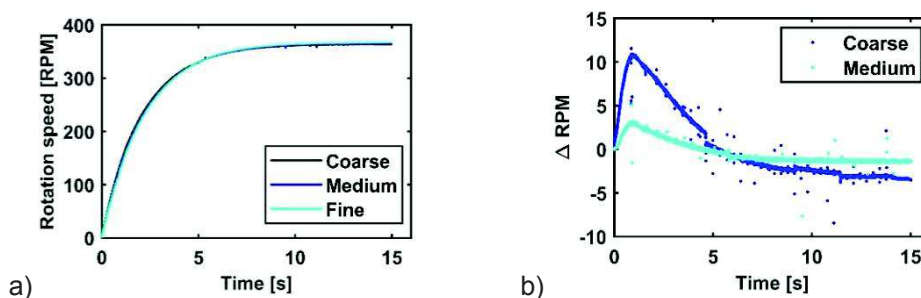## RESULTS AND DISCUSSION

Mesh sensibility analysis

Figure 5. CFD simulation result using three mesh sizes: coarse, medium and fine, for the four-blade propeller with an air velocity of 1.5 m s^{-1}: a) Comparison of the transient response of the four-blade propeller for each mesh size; b) Difference between the rotation speed of the propeller for the fine mesh size with respect to the coarse and medium mesh size.

CFD results of the transient simulation of the four-blade propeller with a simulation time of 15 s are shown in Fig. 5, a. The dynamic behavior of the propellers was similar for all the employed meshes, with final rotation speeds of 363.1, 365.2 and 366.5 RPM, for the coarse, medium and fine mesh sizes, respectively. Assuming as the fine mesh approximate to the real value, the other values present a relative error below 1%, 0.94% and 0.36% for the coarse and medium mesh, respectively. Additionally, according to the computational time required for each mesh size (Table 2), the CFD simulation with coarse mesh require 40% less computational time than the fine mesh and 26.6% less that the medium one. According to this tendency, increasing the mesh size above the fine mesh size has not a significative effect over the final rotational speed but an exponential increasing in the computational time and in the number of the mesh elements. The differences between the rotation speeds of the propeller for the different meshes for 15 s of simulation time are shown in Fig. 5, b. The medium mesh presented the minor difference for all the simulation. Due this, the medium mesh size was selected as the optimal mesh size for the CFD simulations.

Table 2. Number of iterations, computational time and rotation speed of the four-blade propeller for 15 s

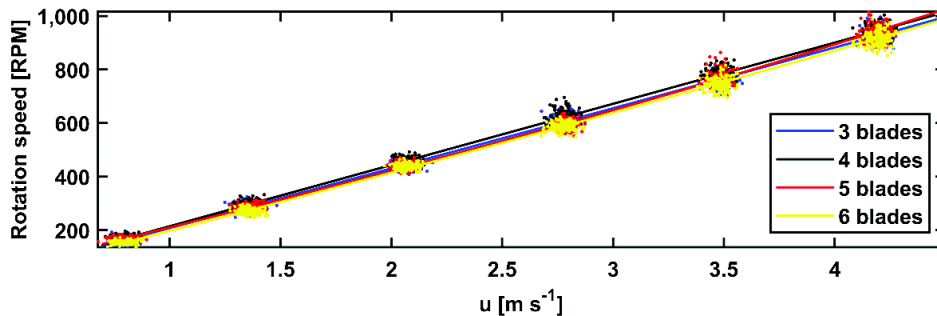|	Mesh size		
	Coarse	Medium	Fine
Number of iterations	120,337	109,221	112,780
Computational time	1,789 min	2,440 min	2,979 min
RPM at 15 s	363.1	365.2	366.5

CFD results and wind tunnel tests

Figure 6. Experimental comparison of the propellers rotation speed.

The comparison between the rotational speeds of the propellers tested in the wind tunnel is shown in Fig. 6. All the anemometers have similar behaviors: a linear relation between the wind speed and the rotation speed as was found early by (Pindado et al., 2012). The four-blade propeller presents the higher rotation speed followed by the three-blade propeller, while the six-blade propeller presented the lower rotation speed. Although the three-blade propeller has the lowest mass, the four-blade propeller take advantage of the aerodynamic torque more efficiently in comparison with the other

937

propellers. At increasing the number of blades, an increase in the surface area of the propeller is achieved, but at the costs of increase the mass of the propeller, decreasing the final rotation speed. All propellers studied start to rotate with an airflow velocity above 0.7 m s^{-1} (threshold speed). In the Table 3, the parameters of the linear fitted equations of the propellers rotation speed with the airflow velocity ($u = a \cdot pps + b$) are presented; where u is the airflow velocity [m s^{-1}], pps is the number of pulses per seconds given by the encoder sensor and b is the fitted curve intercept. All the Pearson's correlation coefficient were above 0.99 and the standard deviation of the revolution speed measure were around 16 RPM for all the anemometers.

Table 3. Coefficient of the fitted linear equation ($u = a \cdot pps + b$) of the propeller rotation speed with the air speed; where u is the air speed [m s^{-1}], pps is the number of pulses per seconds given by the encoder sensor. r² is the Pearson correlation coefficient s is the standard deviation of the rotational speed of each propeller in RPM

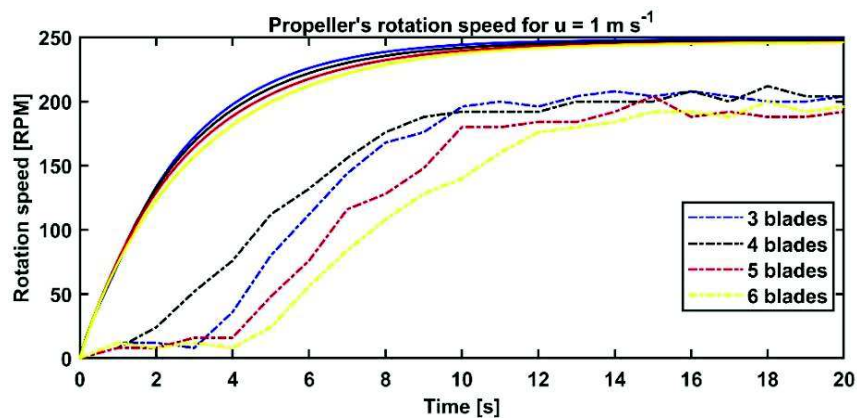|	Number of blades			
	3	4	5	6
a	0.0177	0.01745	0.01751	0.01788
b	0.08942	0.07018	0.1169	0.1294
r²	0.9946	0.9951	0.9937	0.9946
s	16.6	16.0	16.6	15.2

Figure 7. Comparison between the CFD results (solid line) and experimental data (dashed line) for the four propellers studied.

The final rotation speed of the propellers for an airflow velocity of 1 m s^{-1} was compared in the Fig. 7. All the propellers show a similar settling time (around 12 s) for the CFD results, while for the experimental data, the four-blade propeller present the lower settling time among them (around 18 s) and over the CFD results. The final rotation speed for the experimental test was very similar between propellers. The experimental results are up to 37% lower than the results obtained in CFD and the Normalized Mean Square Error (NMSE) computed were 0.31, 0.21, 0.43 and 0.54, for the three to six blade propeller, respectively. This difference could be attributed to the bearing friction torque as was studied by (Pindado et al., 2014), because the CFD model employed do not consider it. The same bearing was used in all experimental tests, just the propellers were interchanged. The four-blade propeller starts to rotate first, with the higher steady-state rotation speed, which leads it to have a lower rising time, as can be seen in Fig. 7. This is an indicative that this propeller is able to generate the higher

938

aerodynamic torque among the all. The steady-state rotation speed for the CFD results and the experimental data, and the Root Mean Square Error (RMSE) computed for all the experimental measurements are presented in the Table 4. The average of the last ten seconds of the steady-state condition was considered as experimental values. The four-blade propeller presents the lower RMSE value among the all.

A comparison between CFD simulation and experimental tests for different airflow velocities is showed in the Fig. 8, a for the four-blade propeller. The relative error (Fig. 8, b) increase exponentially with the air velocity, but tend to stabilized around 12.25%. This value can be explain again, by the lack of the bearing friction torque in the CFD model and because the effect of the rugosity of the material was not consider either.

Table 4. Steady-state rotation speed in RPM for the CFD results and experimental data in RPM and the Root Mean Square Error (RMSE) computed for all the experimental measurements

	Number of blades			
	3	4	5	6
CFD [RPM]	248.5	247.4	246.6	246
Experimental [RPM]	203.64	206.18	205.82	198.55
RMSE [RPM]	129.9	107.4	139.9	147.4

Both effects decrease the aerodynamic torque generate by the propeller and consequently the rotation speed in steady state.
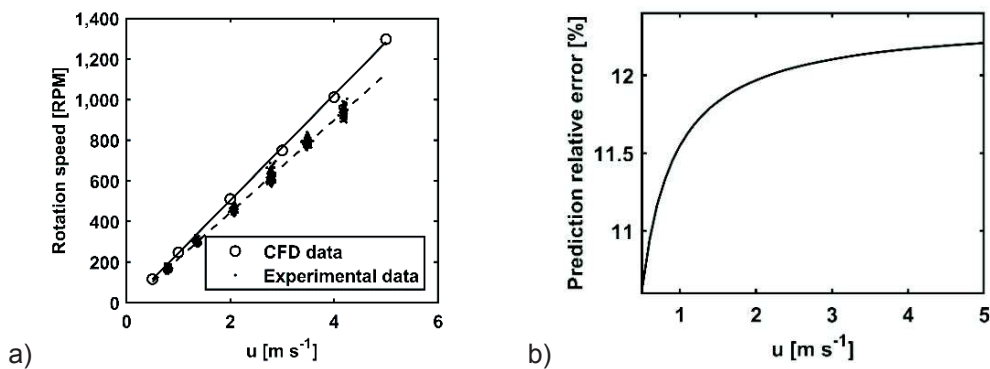

Figure 8. a) Comparison between the CFD results and experimental data for the four-blade anemometer. The solid and dashed lines corresponds to the linear fit to the CFD and experimental results, respectively; b) Prediction relative error between the CFD and experimental results.

Cattle dairy compost barn building tests

A grid of 10 x 6 averaged air velocity measurements was obtained from an area of 126 m^2 below the HVLS fan and from an area of 108 m^2 below and in front of the LVHS fan. Surface functions were fitted to the measurements employing a thin plate spline interpolation (Keller & Borkowski, 2019) by mean of MATLAB® software. A grid of 100x100 points were evaluated for each surface to obtain a detailed behavior of the airflow velocity distribution in the area of study.

The averaged air velocity distribution due to the HVLS fan operation is shown in Fig. 9. The air flow was distributed around the fan with a low airflow velocity zone of approximately 2.5 m of diameter locate right below the fan, as was also found by (Perez Fagundes, 2016). It is also noticed a zone at the right side of the fan with a low airflow velocity, relate to an adjacent hill near to the right side of the facility, which affect the airflow distribution pattern. The minimum and maximum average airflow velocities were 0.48 and 3.48 m s^{-1}, respectively.
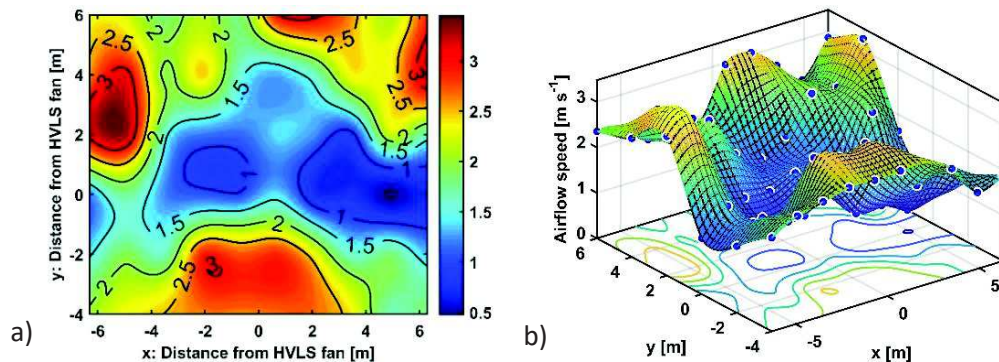

Figure 9. Contour map and surface map of the averaged airflow velocity distribution measured at 0.5 m above the dairy compost bed for a HLVS fan.

The averaged air velocity distribution due to the LVHS fan operation is shown in Fig. 10. The maximum airflow velocity was presented at 2 meters in front of it and the airflow velocity decrements to the sides, covering the entire width. The airflow velocity decreased to 1.4 m s^{-1} at 8 m from the fan. The LVHS presented a low airflow velocity zones below of the fan and to the sides, spreading up to 4 meters. The airflow distribution has a cone shape, which is characteristic of high-speed fans. The minimum and maximum average airflow velocities obtained were 0.22 and 3.39 m s^{-1}, respectively.
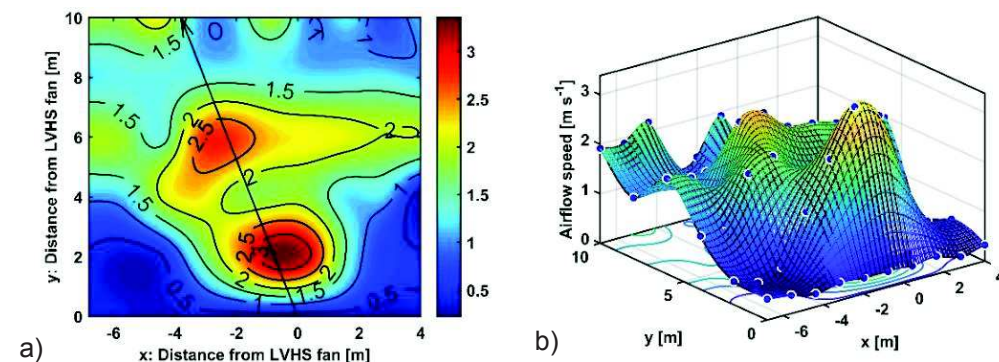

Figure 10. Contour map (a) and surface map (b) of the average airflow velocity distribution measured at 0.5 m above the dairy compost bed for a LVHS fan. The arrow in the contour map indicates the direction in which the fan is oriented.

Eqs (1) and (2) were developed to compute the fans ventilation area coverage (VAC) for a minimum airflow velocity and for an interval airflow velocity inside the compost dairy barns. Where n and m are the number of elements of the grid for each spatial dimension (x and y); u_{min} is the minimum airflow velocity for which the VAC is computed; u_{ij} is the airflow velocity in the coordinate (i, j) inside the grid; Δu is the amplitude of the airflow velocity interval around a specific airflow velocity for which the VAC is computed; ΔA is the area of each element of the grid and A is the area of the grid.

$$VAC_k = \frac{\Delta A}{A} \sum_{i=1}^{n} \sum_{j=1}^{m} f\left(u_{ij}, U_k\right) \ where \ f\left(u_{ij}, u_{min}\right) = \begin{cases} 1 & if \ u_{ij} \geq u_{min_k} \\ 0 & otherwise \end{cases} \tag{1}$$

$$VAC_k = \frac{\Delta A}{A} \sum_{i=1}^{n} \sum_{j=1}^{m} g\left(u_{ij}, U_k\right) \ where \ g\left(u_{ij}, U_k\right) = \begin{cases} 1 & if \ |u_{ij} - U_k| \leq \Delta u \\ 0 & otherwise \end{cases} \tag{2}$$

The average area coverage relate to a specific minimum airflow velocity is shown in the Fig. 11. This is which ventilation area percentage present an airflow velocity above an specific value (u_{min}); i.e. a ventilation area coverage of 89.62% and 77.05% have an airflow velocity above 1 m s^{-1} for the HVLS and LVHS fans, respectively. Between the two fans, exist a difference up to 20% in the ventilation area coverage, being the HVLS fan the one with the greater ventilation area coverage for a particular minimum airflow velocity.
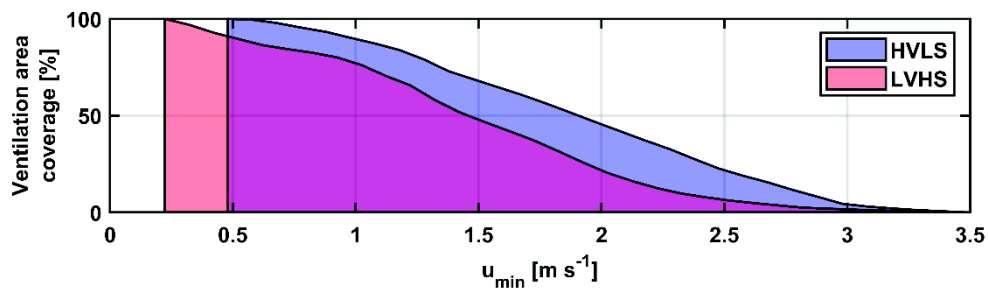

Figure 11. Ventilation area coverage that present airflow velocities above a specific value (u_{min}).
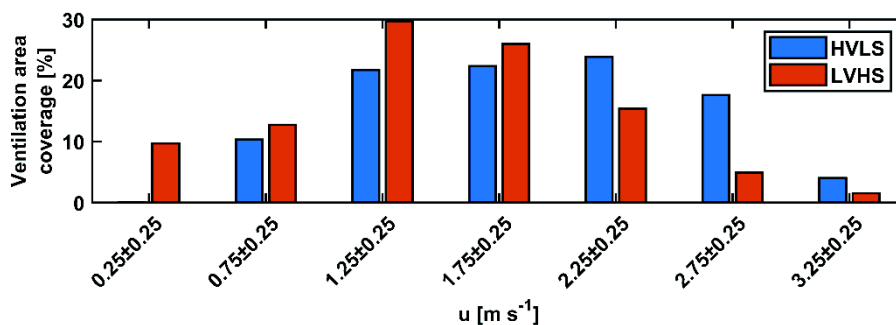

Figure 12. Ventilation area coverage with respect to specific ranges of airflow velocities.

The ventilation area coverage with respect to specific ranges of airflow velocities is shown in Fig. 12. An average airflow velocity between 0 and 0.5 m s^{-1} for the LVHS fan covers 10% of the studied area. Meanwhile an airflow velocity between 0.5 and 1 m s^{-1} for the HVLS fan covers 12.5% of the studied area; this fan not present lower airflow velocities values. The HVLS present a uniform ventilation area coverage between 22% and 24% for airflow velocities between 1 and 2.5 m s^{-1}. However, for the LVHS fan, the ventilation area coverage change considerably for the same airflow velocity range, from 30% to 15%, being the 1 to 1.5 m s^{-1} range the one that cover the greatest area. The total ventilation area coverage in the range of 1 to 2.5 m s^{-1} were 68.01% and 77.55% for the HVLS and LVHS fans, respectively. However, for the airflow velocities above this range, the ventilation area coverage descent markedly to 6.43% and 21.61% for the LVHS and the HVLS system, respectively.

Those results suggest that the HVLS fan present the best airflow distribution at the measured airflow velocity level, covering all the studied area with airflow velocities above 0.5 m s^{-1} while the LVHS fan cover 90.29% of the studied area for the same airflow velocities. The 9.71% missing area is located mainly below and to the sides of the LVHS fan. Damasceno et al. (2019) suggested that an airflow velocity above 1.8 m s^{-1} could guarantee the proper drying of the compost bed. With this study, was possible to determine that the HVLS and LVHS fans present a ventilation area coverage of 55.2% and 33.1%, respectively, for airflow velocities above this value. This must be consider when selecting the ventilation system of the compost dairy barns, because this lack of air distribution homogeneity not only could lead to poor drying of the compost in certain location of the compost barn as was discussed by (Black et al., 2013), but also affect the bioclimatic condition of livestock.

CONCLUSIONS

This paper proposed a feasible low-cost 3D printed anemometer network to characterize the airflow distribution inside closed-field agricultural production systems. The developed anemometers were simulated using the innovative CFD/6-DOF models allowing to determine their dynamic response to specific air conditions. Using the proposed anemometer network it was possible to compare the air flow distribution pattern of two compost stables with different fan configurations. Being the high-volume low-speed fan configuration which presented the best airflow distribution homogeneity.

To select the most suitable sensor for the measurement, comparison with a theoretical value was employed. For this purpose a model was simulated. The developed model can be improved, to give more realistic values, if the friction torque and inertia forces are considered in the equation. Even though, the low-cost anemometer network can be consider as a useful tool to determine airflow distribution in agricultural facilities with air velocities over 0.7 m s^{-1}. In the case of compost dairy facilities with mechanical ventilations, it can be used as a diagnostic tool to study the heterogeneity of the air distribution near the compost surface in real time, providing important scientific and industrial information.

The developed tool and proposed methodology allow highlighting the zones with low airflow velocity, making possible to determine if the capacity, location or orientation of the fan are in agreement with the requirements of the facility. At compare the airflow

distribution measured with a previously airflow distribution is possible to detect fails in the ventilation system, as a decrement in the ventilation efficiency of the fans.

REFERENCES

Ansys Inc. 2016. *ANSYS Fluent User's Guide, Release 17.2*.

ASTM. 2019. *ASTM D5157-19, Standard Guide for Statistical Evaluation of Indoor Air Quality Models*.

Black, R.A., Taraba, J.L., Day, G.B., Damasceno, F.A. & Bewley, J.M. 2013. Compost bedded pack dairy barn management, performance, and producer satisfaction. *Journal of Dairy Science* **96**(12), 8060–8074. https://doi.org/10.3168/jds.2013-6778

Bustamante, E., Calvet, S., Estellés, F., Torres, A.G. & Hospitaler, A. 2017. Measurement and numerical simulation of single-sided mechanical ventilation in broiler houses. *Biosystems Engineering* **160**, 55–68. https://doi.org/10.1016/j.biosystemseng.2017.05.009

Bustamante, E., García-Diego, F.J., Calvet, S., Torres, A.G. & Hospitaler, A. 2015. Measurement and numerical simulation of air velocity in a tunnel-ventilated broiler house. *Sustainability (Switzerland)* **7**(2), 2066–2085. https://doi.org/10.3390/su7022066

Calvet, S., Cambra-López, M., Blanes-Vidal, V., Estellés, F. & Torres, A. G. 2010. Ventilation rates in mechanically-ventilated commercial poultry buildings in Southern Europe: Measurement system development and uncertainty analysis. *Biosystems Engineering* **106**(4), 423–432. https://doi.org/10.1016/j.biosystemseng.2010.05.006

Camuffo, D. 2019. Measuring Wind and Indoor Air Motions. In *Microclimate for Cultural Heritage* (Third Edit, pp. 483–511). Elsevier. https://doi.org/10.1016/b978-0-444-64106-9.00020-1

Damasceno, F.A., Oliveira, C.E.A., Ferraz, G.A.S., Nascimento, J.A.C., Barbari, M. & Ferraz, P.F.P. 2019. Spatial distribution of thermal variables, acoustics and lighting in compost dairy barn with climate control system. *Agronomy Research* **17**(2), 385–395. https://doi.org/10.15159/AR.19.115

Dunbar, A.J., Craven, B.A. & Paterson, E.G. 2015. Development and validation of a tightly coupled CFD/6-DOF solver for simulating floating offshore wind turbine platforms. *Ocean Engineering* **110**, 98–105. https://doi.org/10.1016/j.oceaneng.2015.08.066

Fiedler, M., Berg, W., Ammon, C., Loebsin, C., Sanftleben, P., Samer, M., von Bobrutzki, K., Kiwan, A. & Saha, C.K. 2013. Air velocity measurements using ultrasonic anemometers in the animal zone of a naturally ventilated dairy barn. *Biosystems Engineering* **116**(3), 276–285. https://doi.org/10.1016/j.biosystemseng.2012.10.006

Gao, Y., Ramirez, B.C. & Hoff, S.J. 2016. Omnidirectional thermal anemometer for low airspeed and multi-point measurement applications. *Computers and Electronics in Agriculture* **127**, 439–450. https://doi.org/10.1016/j.compag.2016.06.011

Keller, W. & Borkowski, A. 2019. Thin plate spline interpolation. *Journal of Geodesy* **93**(9), 1251–1269. https://doi.org/10.1007/s00190-019-01240-2

Kiwan, A., Berg, W., Brunsch, R., Özcan, S., Müller, H.J., Gläser, M., Fiedler, M., Ammon, C. & Berckmans, D. 2012. Tracer gas technique, air velocity measurement and natural ventilation method for estimating ventilation rates through naturally ventilated barns. *Agricultural Engineering International: CIGR Journal* **14**(4), 22–36.

Leoni, A., Stornelli, V. & Pantoli, L. 2018. A low-cost portable spherical directional anemometer for fixed points measurement. *Sensors and Actuators, A: Physical* **280**, 543–551. https://doi.org/10.1016/j.sna.2018.08.025

Luck, B.D., Davis, J.D., Purswell, J.L., Kiess, A.S., Hoff, S.J. & Olsen, J.W.W. 2014. Effect of measurement density on characterizing air velocity distribution in commercial broiler houses. *Transactions of the ASABE* **57**(5), 1443–1454. https://doi.org/10.13031/trans.57.10409

Obando Vega, F.A., Montoya Ríos, A.P., Osorio Saraz, J.A., Vargas Quiroz, L.G. & Alves Damasceno, F. 2020. Assessment of black globe thermometers employing various sensors and alternative materials. *Agricultural and Forest Meteorology* **284**(August 2019), 107891. https://doi.org/10.1016/j.agrformet.2019.107891

Perez Fagundes, B. 2016. *Determinação do fluxo de ar mais homogêneo, comparativo a dois sistemas de ventilação forçada por ventiladores, aplicados em galpões de confinamento de vacas leiteiras em sistemas de camas de compostagem (compost barn)*. Faculdade Profissional - Curitiba.

Pindado, S., Cubas, J. & Sorribes-Palmer, F. 2014. The cup anemometer, A fundamental meteorological instrument for the wind energy industry. Research at the IDR/UPM institute. In *Sensors (Switzerland)* (Vol. **14**, Issue 11). https://doi.org/10.3390/s141121418

Pindado, S., Sanz, A. & Wery, A. 2012. Deviation of cup and propeller anemometer calibration results with air density. *Energies* **5**(3), 683–701. https://doi.org/10.3390/en5030683

Samer, M., Loebsin, C., von Bobrutzki, K., Fiedler, M., Ammon, C., Berg, W., Sanftleben, P. & Brunsch, R. 2011. A computer program for monitoring and controlling ultrasonic anemometers for aerodynamic measurements in animal buildings. *Computers and Electronics in Agriculture* **79**(1), 1–12. https://doi.org/10.1016/j.compag.2011.08.006

Shamshiri, R. 2017. Measuring optimality degrees of microclimate parameters in protected cultivation of tomato under tropical climate condition. *Measurement* **106**, 236–244. https://doi.org/10.1016/j.measurement.2017.02.028

Shamshiri, R. & Ismail, W.I.W. 2012. Performance Evaluation of Ventilation and Pad-and-Fan Systems for Greenhouse Production of Tomato in Lowland Malaysia. *World Research Journal of Agricultural & Biosystems Engineering* **1**(1), 1–5. http://www.bioinfo.in/contents.php?id=250

Shamshiri, R.R., Kalantari, F., Ting, K.C., Thorp, K.R., Hameed, I.A., Weltzien, C., Ahmad, D. & Shad, Z. 2018. Advances in greenhouse automation and controlled environment agriculture: A transition to plant factories and urban agriculture. *International Journal of Agricultural and Biological Engineering* **11**(1), 1–22. https://doi.org/10.25165/j.ijabe.20181101.3210

Shamshiri, R.R., Mahadi, M.R., Thorp, K.R., Ismail, W.I.W., Ahmad, D. & Man, H.C. 2017. Adaptive Management Framework for Evaluating and Adjusting Microclimate Parameters in Tropical Greenhouse Crop Production Systems. In *Plant Engineering*. INTECH. https://doi.org/10.5772/intechopen.69972

van Dooren, H.J.C. & Sapounas, A. 2013. *Use of computational fluid dynamics (CFD) modelling to improve tracer gas techniques in very open naturally ventilated livestock buildings* (Issue September).

Vilela, M.O., Gates, R.S., Martins, M.A., Barbari, M., Conti, L., Rossi, G., Zolnier, S., Teles, C. G.S., Zanetoni, H.H.R., Andrade, R.R. & Tinôco, I.F.F. 2019. Computational fluids dynamics (CFD) in the spatial distribution of air velocity in prototype designed for animal experimentation in controlled environments. *Agronomy Research* **17**(3), 890–899. https://doi.org/10.15159/AR.19.108

Zajicek, M. & Kic, P. 2012. Improvement of the broiler house ventilation using the CFD simulation. *Agronomy Research* **10**(SPEC. ISS. 1), 235–242.